Detection of nitrogen gas in the β Pictoris circumstellar disc

Wilson, P.A.; Kerr, R.; Lecavelier des Etangs, A.; Bourrier, V.; Vidal-Madjar, A.; Kiefer, F.; Snellen, I.A.G.

Citation

Wilson, P. A., Kerr, R., Lecavelier des Etangs, A., Bourrier, V., Vidal-Madjar, A., Kiefer, F., & Snellen, I. A. G. (2019). Detection of nitrogen gas in the β Pictoris circumstellar disc. *Astronomy And Astrophysics (0004-6361)*, *621*, A121. doi:10.1051/0004-6361/201834346

Astronomy & Astrophysics manuscript no. N
November 14, 2018

Detection of Nitrogen gas in the β Pictoris circumstellar disk

P. A. Wilson[1, 2, 3, 4], R. Kerr[5], A. Lecavelier des Etangs[3, 4], V. Bourrier[3, 4, 6],
A. Vidal-Madjar[3, 4], F. Kiefer[3, 4], and I. A. G. Snellen[2]

[1] Department of Physics, University of Warwick, Coventry CV4 7AL, UK
e-mail: `paul.a.wilson@warwick.ac.uk`
[2] Leiden Observatory, Leiden University, Postbus 9513, 2300 RA Leiden, The Netherlands
[3] CNRS, UMR 7095, Institut d'Astrophysique de Paris, F-75014, Paris, France
[4] Institut d'Astrophysique de Paris, F-75014, Paris, France
[5] University of British Columbia, 2329 West Mall, Vancouver, BC, V6T 1Z4, Canada
[6] Observatoire de l'Université de Genève, 51 chemin des Maillettes, 1290 Sauverny, Switzerland

Received August 29, 2018; accepted November 9, 2018

ABSTRACT

Context. The debris disk surrounding β Pictoris has a gas composition rich in carbon and oxygen, relative to solar abundances. Two possible scenarios have been proposed to explain this enrichment. The preferential production scenario suggests that the gas produced may be naturally rich in carbon and oxygen, while the alternative preferential depletion scenario states that the enrichment has evolved to the current state from a gas with solar-like abundances. In the latter case, the radiation pressure from the star expels the gas outwards, leaving behind species less sensitive to stellar radiation such as C and O. Nitrogen is also not sensitive to radiation pressure due to its low oscillator strength, which would make it also overabundant under the preferential depletion scenario. As such, the abundance of nitrogen in the disk may provide clues to why C and O are overabundant.

Aims. We aim to measure the nitrogen column density in the direction of β Pictoris (including contributions by the interstellar medium and circumstellar disk), and use this information to disentangle these different scenarios explaining the C and O overabundance.

Methods. Using far-UV spectroscopic data collected by the *HST*'s *Cosmic Origins Spectrograph* (COS) instrument, we analyse the spectrum and characterise the NI triplet by modelling the absorption lines.

Results. We measure the nitrogen column density in the direction of β Pictoris for the first time, and find it to be $\log(N_{\mathrm{NI}}/1\,\mathrm{cm}^2) = 14.9 \pm 0.7$. The nitrogen gas is found to be consistent with solar abundances and Halley dust. We also measure an upper limit for the column density of MnII in the disk at $\log(N_{\mathrm{MnII}}/1\,\mathrm{cm}^2)_{\mathrm{CS}} = 12.7^{+0.1}$ and calculate the column density of SIII** in the disk to be $\log(N_{\mathrm{SIII}^{**}}/1\,\mathrm{cm}^2)_{\mathrm{CS}_X} = 14.2 \pm 0.1$. Both results are in good agreement with previous studies.

Conclusions. The solar nitrogen abundance supports the preferential production hypothesis, in which the composition of gas in β Pictoris is the result of photodesorption from icy grains rich in C and O or collisional vaporisation of C and O rich dust in the disk. It does not support the hypothesis that C and O are overabundant due to the insensitivity of C and O to radiation pressure thereby leaving them to accumulate in the disk.

Key words. stars: early-type – stars: individual: β Pictoris – circumstellar matter

1. Introduction

β Pictoris (β Pic) is a young 23 ± 3 Myr (Mamajek & Bell 2014) planetary system which hosts a near edge-on debris disk composed of dust and gas. The gas in the disk is not thought to be primordial, but rather continually replenished through evaporation and collisions between dust grains. The detection of the CO molecule (Vidal-Madjar et al. 1994; Dent et al. 2014; Matrà et al. 2017), is evidence that new gas is being produced. This is because of the very short, ~ 120 year typical lifetime of the CO molecule (Visser et al. 2009). The presence of UV photons from the ambient interstellar medium rapidly dissociates CO into C and O, which then evolves by viscous spreading (Kral et al. 2016, 2017).

Observations have shown that the circumstellar (CS) disk has a particularly large overabundance of C and O relative to a solar abundance (Roberge et al. 2006; Brandeker 2011). Xie et al. (2013) introduced two opposing hypotheses for explaining the origin of this overabundance. The first hypothesis, which they named *preferential production*, occurs when the gas is produced with an enriched C and O abundance. Such an enrichment could be created through processes which release gas from solid bodies with an inherently high C and O abundance, such as bodies rich in CO (Kral et al. 2016). The main gas producing processes are photodesorption off the grains; a non-thermal desorption mechanism which releases gas by UV-flux (Grigorieva et al. 2007); collisional vaporisation of the dust in the disk (Czechowski & Mann 2007); cometary collisions (Zuckerman & Song 2012); and sublimating exocomets (Ferlet et al. 1987; Beust et al. 1990; Lecavelier Des Etangs et al. 1996). *Preferential depletion*, the second of the two hypotheses by Xie et al. (2013), suggests that the gas evolves to have an elevated C and O abundance from an original solar abundance ($\gtrsim$ 1 dex). Metallic elements subject to strong radiation forces, such as Na and Fe, could deplete more quickly than C and O for which the radiation force is negligible, which would lead to an overabundance of C and O. The presence of the overabundant C and O has been invoked as an explanation for why other gas species seen in the CS disk have not been blown away by the radiation pressure of the star and why the orbital motion of the gas is consistent with Keplerian rotation (Fernández et al. 2006).

A column density measurement of nitrogen could help disentangle these two hypotheses for explaining the overabundance of C and O. If the N/Fe column density is found to comparable to N/Fe solar abundance, this will speak in favour of *preferential production*. If the column density of N is found to be high, this could support the *preferential depletion* hypothesis. This is because N, like C and O, is not sensitive to radiation forces and thus should under the *preferential depletion* scenario be overabundant compared to radiation-sensitive species.

A column density measurement of N might also shed light on the gas production mechanism in the β Pic CS disk. Molecular abundance analyses of comets in the Solar System indicate that cometary coma consist mostly of H_2O ($\sim$ 90%) followed by CO ($\sim$ 5%) and $CO_2 \sim 3\%$ and that Nitrogen-bearing molecules such as N_2, NH_3, and CN are only minor constituents (e.g. Krankowsky et al. 1986; Eberhardt et al. 1987; Wyckoff et al. 1991). Although these studies have measured the cometary coma and not the internal abundances, it is unlikely that comets should produce significant amounts of N.

In this paper, we present the first detection of nitrogen in the β Pic disk based upon observations obtained using the Hubble Space Telescope (*HST*) together with the far-UV Cosmic Origins Spectrograph (COS) instrument. In Sect. 2 we present the observational setup and technique used. The analysis of the data, which includes airglow removal, spectral alignment, and the combination and modelling of the NI lines is presented in Sect. 3. The results are presented in Sect. 4 with a discussion of the obtained NI abundance measurements in Sect. 5. The main findings and significance of the NI abundance measurement is summarised in Sect. 6.

2. Observations

The far-UV observations of β Pic were obtained using the *Cosmic Origins Spectrograph (COS)* on the *Hubble Space Telescope (HST)* using the TIME-TAG mode and the G130M grating. The observations were done using the primary science aperture, which has a 2.5 $''$ diameter field stop. The observations consisted of a total of 11 visits and 31 orbits, conducted between February 2014 and May 2018. The central wavelength was first set at 1291 Å however, upon inspection of the data, a decision was made to change the central wavelength setting to 1327 Å for all observations after 2016 to avoid the photon poor region towards the shortest wavelengths. The two central wavelength positions overlap in the 1171 - 1279 Å and 1327 - 1433 Å wavelength regions.

To avoid contamination by geocoronal emission (airglow) we use the Airglow Virtual Motion (AVM) technique where the target is deliberately offset along the dispersion axis thereby separating the target spectrum from the stationary airglow spectrum. A more detailed description method of this method can be found in the Appendix section of Wilson et al. (2017). The data were all reduced using the `COSTOOLS` pipeline (Fox et al. 2015) version 3.2.1 (2017-04-28).

3. Analysis

3.1. Airglow modelling and subtraction

The Hubble Space Telescope is located in Earth's tenuous atmosphere (in the exosphere) where H, N and O is present in sufficient quantities to be detected in emission at far-UV wavelengths. These emission lines, known as airglow, are present in the data, and can, if left un-corrected, reduce the accuracy of the column density estimates. We remove the airglow contamination by subtracting an airglow template made from combining several airglow-only observations. The airglow templates were created using data obtained during our previous observations (Wilson et al. 2017) in combination with airglow templates made available on the Space Telescope Science Institute (STScI) website[1].

The final airglow-subtracted data, F, were created by subtracting the airglow template, F_{AG}, scaled by a factor C, from the original contaminated data spectrum, F_{tot}. This is expressed in the following equation:

$$F = F_{\mathrm{tot}} - C \times F_{\mathrm{AG}}. \tag{1}$$

A detailed explanation of these latter steps, including the methods for calculating C, are explained in the Appendix sections A.1 - A.3.

3.2. Choice of line spread function

Mid-frequency errors caused by polishing irregularities in the HST primary and secondary mirrors causes the spectroscopic line-spread function (LSF) to exhibit extended wings with a core that is broader and shallower when compared to a Gaussian LSF. For our modelling we chose to use the tabulated LSF (LP3) available on the STScI website[2]. Since the shape of the LSF changes with wavelength we chose the tabulated LSF closest to our wavelength region of interest: G130M/1222. The shape of the LSF reduces our ability to detect faint and narrow spectral features. It is therefore likely that we are not particularly sensitive to the fainter MnII and SiII** which exist close to the NI lines. Furthermore, the non-Gaussian line wings also mak it hard to detect closely spaced narrow spectral features. This limits the complexity of our model to only a few absorption components.

3.3. Modelling the NI lines

The NI absorption lines in the β Pic spectrum were modelled using Voigt profiles. We compute the Voigt profile (a convolution of a Gaussian and a Lorentzian profile) as the real part of the Faddeeva function, computed with standard Python libraries (`scipy.special.wofz`). Each nitrogen line in the main triplet (1199.5496, 1200.2233 and 1200.7098 Å) was modelled and fit simultaneously over a predefined spectral region (1198.48 - 1202.35 Å). The additional NI triplet at (1134.1653, 1134.4149 and 1134.9803 Å) towards the end of the detector and the weak lines at 1159.8168 and 1160.9366 Å have weak line strengths which results in line depths which lie below the local noise level, so they were not included in the fitting. Once we found a satisfactory model for the main NI triplet at $\sim$ 1200 Å we compare this solution with the other weaker NI line regions and find that our model is consistent with these much weaker lines. We also modelled the MnII and SiII** lines at 1199.39, 1201.12 Å and 1200.97 Å respectively as they partially overlap with the NI lines. The separate SiII** line at 1201.73 Å was used to break any degeneracy between the NI line at 1200.71 Å and the SiII** line at 1200.97 Å.

---

[1] `http://www.stsci.edu/hst/cos/calibration/airglow.html`

[2] `http://www.stsci.edu/hst/cos/performance/spectral_resolution/`

3.3.1. Choosing the number of model components

We initially fit the absorption lines using a two component model consisting of one component representing the interstellar medium (ISM) and another the circumstellar gas disk. The resulting fit was poor, suggesting the presence of a third component. This third component is added and named $\mathrm{CS_X}$, and its inclusion decreased the value of the reduced χ^2 from 1.6 (with 10 free parameters) to 1.0 (with 15 free parameters). This decreased the Bayesian information criterion (Schwarz et al. 1978) from 646 to 451 and the Akaike information criterion (Akaike 1974) from 607 to 409. Adding a fourth component, however, did not improve the fit, so we settle on this three-component model. The $\mathrm{CS_X}$ component, which was free to vary in radial velocity space, gave the best fit close to the rest frame of β Pic at 20.0 km/s (Gontcharov 2006; Brandeker et al. 2004). The continuum was modelled using a second order polynomial.

3.3.2. Selecting the free component parameters

In the absence of reliable lines for which to check the wavelength calibration locally, we take the liberty of not constraining the ISM (v_{ISM}) and $\mathrm{CS_0}$ ($v_{\mathrm{CS_0}}$) bulk velocities to their literature values. However, since the ISM component has been well-constrained in previous studies to be offset by -10 km/s relative to the star's radial velocity component (Vidal-Madjar et al. 1994; Lallement et al. 1995), we set this requirement and allow the two parameters to vary together, provided that $v_{\mathrm{CS_0}} - v_{\mathrm{ISM}} = 10\,\mathrm{km/s}$ is maintained. Aside from that constraint, all parameters for the ISM absorption component were kept fixed except for the ISM nitrogen column density, $\log(N_{\mathrm{NI}}/1\,\mathrm{cm}^2)_{\mathrm{ISM}}$. The fixed ISM parameters were $T_{\mathrm{ISM}} = 7000\,\mathrm{K}$ (the temperature of the ISM) and $\xi_{\mathrm{ISM}} = 1.5\,\mathrm{km/s}$ (the turbulent broadening of the ISM), both values of which follow from studies observing the interstellar medium towards β Pic and other nearby stars, such as Bertin et al. (1995); Lallement et al. (1995).

For both circumstellar components, the column density and turbulent broadening (ξ) were set as free parameters. The bulk velocity of the $\mathrm{CS_X}$ component was also allowed to vary freely. The temperature of the CS gas is unknown. However, to avoid the degeneracy introduced when modelling both the turbulent velocity and the temperature simultaneously we fix the CS gas temperature to 10 K for both CS components. The relationship between the parameters are expressed mathematically as

$$b^2 = \frac{2kT}{m} + \xi^2 \tag{2}$$

where b is the width of the lines, T the temperature, k, the Boltzmann constant, m the mass of the considered species and ξ the turbulent broadening (also sometimes referred to as microturbulent velocity).

3.4. Fit to the data

We fit the NI triplet in conjunction with the MnII and SIII** lines with MnII overlapping the blue side of bluest NI line. We do not model SIII** in the ISM component as sulphur will instead exist in the form of SII. We checked and found that only a model with a low SIII** column density provides a fit consistent with the data.

We employed a least squares optimisation to the data using the `scipy.optimize.leastsq` package (Jones et al. 2001–) to obtain initial starting parameters for a Markov chain Monte Carlo (MCMC) run using the `emcee` code described in Foreman-Mackey et al. (2013). We ran 200 MCMC walkers with a total of 10,100 steps each, with 100 burn in steps. This resulted in a total of two million steps, of which ~ 25 % were accepted. The posterior probability distributions for the free model parameters are shown in the corner plot (Foreman-Mackey 2016) in Fig. 3, along with the marginalised 1D distributions which were used to calculate the median values and the uncertainties on each free parameter (see Table 1).

Table 1. The medium values and uncertainties of the posterior probability distributions generating using the MCMC method.

Parameter	Value
Absorption by the ISM	
$\log(N_{\mathrm{NI}}/1\,\mathrm{cm}^2)_{\mathrm{ISM}}$	$13.8^{+0.2}_{-0.3}$
$\log(N_{\mathrm{MnII}}/1\,\mathrm{cm}^2)_{\mathrm{ISM}}$	$\leq 11.0^{+0.7}$
T_{ISM}	$7000\,\mathrm{K}^{\dagger}$
b_{ISM}	$1.5\,\mathrm{km/s}^{\dagger}$
v_{ISM}	$13.3^{+1.8}_{-3.0}\,\mathrm{km/s}$
Narrow absorption by gas at β Pic system velocity, $\mathrm{CS_0}$	
$\log(N_{\mathrm{NI}}/1\,\mathrm{cm}^2)_{\mathrm{CS_0}}$	14.9 ± 0.7
$\log(N_{\mathrm{SIII^{**}}}/1\,\mathrm{cm}^2)_{\mathrm{CS_0}}$	$\leq 11.6^{+0.4}$
$\log(N_{\mathrm{MnII}}/1\,\mathrm{cm}^2)_{\mathrm{CS_0}}$	$\leq 12.2^{+0.1}$
$b_{\mathrm{CS_0}}$	$1.0^{+0.4}_{-0.3}\,\mathrm{km/s}$
$v_{\mathrm{CS_0}}$	$v_{\mathrm{ISM}} + 10\,\mathrm{km/s}$
Broad absorption by gas at β Pic system velocity, CS_X	
$\log(N_{\mathrm{NI}}/1\,\mathrm{cm}^2)_{\mathrm{CS}_X}$	14.04 ± 0.03
$\log(N_{\mathrm{SIII^{**}}}/1\,\mathrm{cm}^2)_{\mathrm{CS}_X}$	14.2 ± 0.1
$\log(N_{\mathrm{MnII}}/1\,\mathrm{cm}^2)_{\mathrm{CS}_X}$	$\leq 12.6^{+0.1}$
b_{CS_X}	$25.8 \pm 1.7\,\mathrm{km/s}$
v_{CS_X}	$25 \pm 1\,\mathrm{km/s}$

† indicates the fixed parameters.

4. Results

4.1. Saturated NI lines

The results from the best fit (and MCMC) show that the $\mathrm{CS_0}$ component is completely saturated (seen by the cyan coloured lines which reach a flux of 0 in Fig. 1). The ISM component is partially saturated. The saturation leads to larger uncertainties on $\log(N_{\mathrm{NI}}/1\,\mathrm{cm}^2)_{\mathrm{CS_0}}$ reaching a magnitude uncertainty of 0.7. This is because an increase in column density doesn't make the absorption signature much deeper, but instead widens the absorption profile which is then partially absorbed by the CS_X component. This is seen by the broad posterior distribution of ξ_{CS_X} values shown in Fig. 3. Interestingly, although the CS_X is free to vary in radial velocity it has the same radial velocity as the $\mathrm{CS_0}$ component (within 1σ). The same bulk velocity values indicates that the $\mathrm{CS_0}$ and CS_X could be describing the same gas. This is discussed more in the discussion (§ 5).

We find a system velocity for β Pic of $23.3^{+1.8}_{-3.2}\,\mathrm{km/s}$ which is consistent with accepted value of ~ 20.5 km/s (Hobbs et al. 1985; Brandeker et al. 2004). The slight difference between the

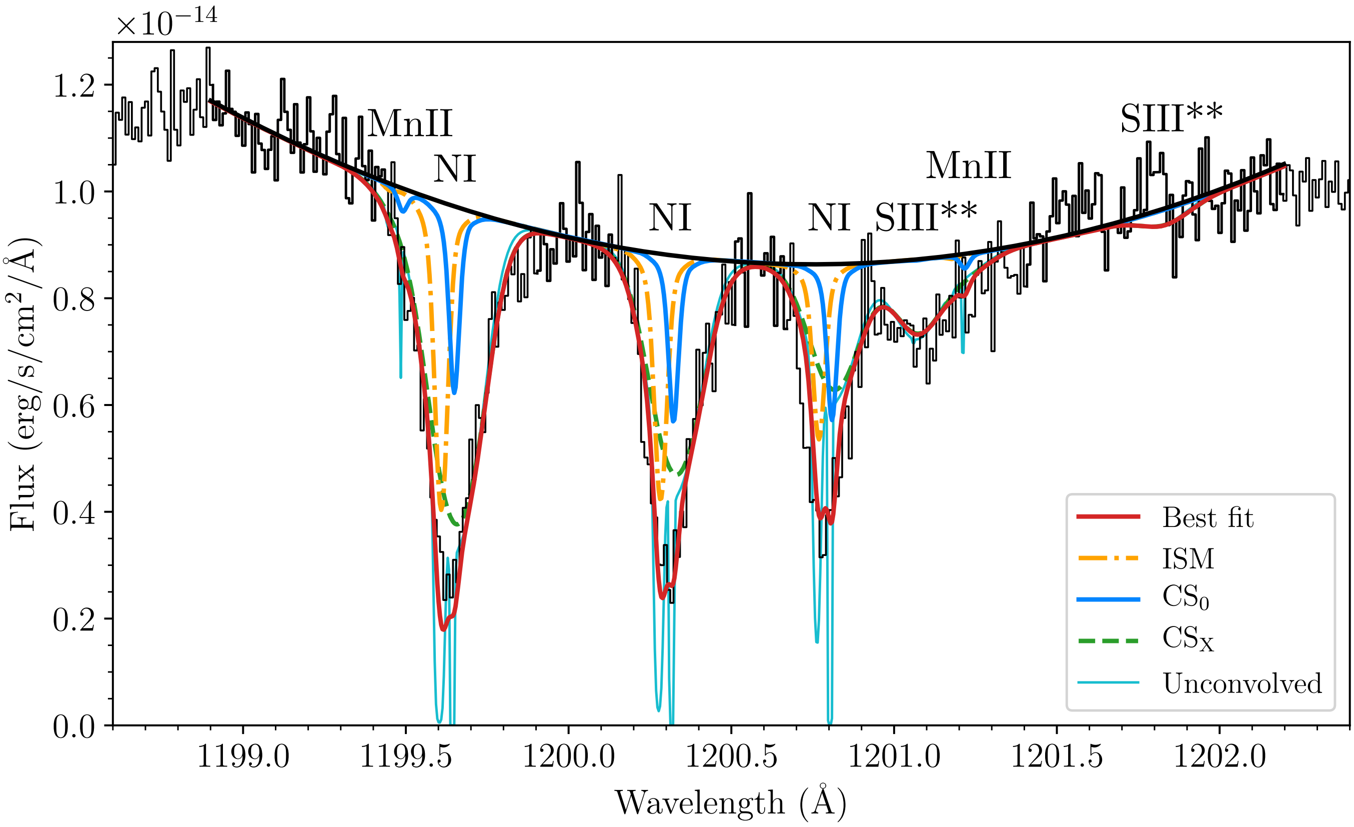

Fig. 1. Measured flux as a function of wavelength (HST rest frame) for the NI lines at ∼ 1200 Å. The black spectrum represents the combined data with the thicker parts indicating the region used to fit the continuum which is shown as a black solid line. The coloured lines show the individual components with the cyan coloured line showing the individual absorption profiles before they get convolved by the instrumental LSF.

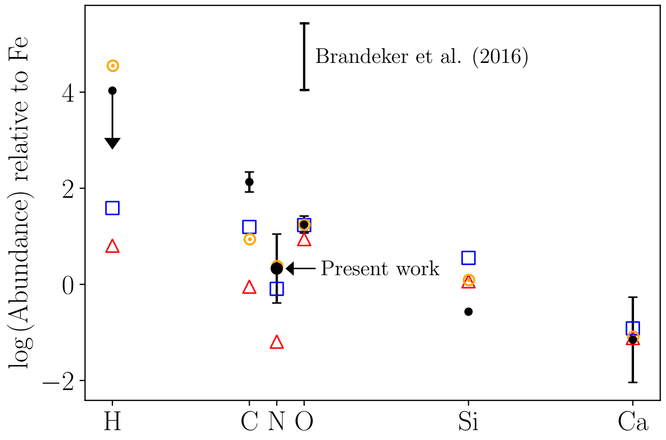

Fig. 2. The abundances of the β Pic gas disk (black circles) compared to solar abundances (orange Sun symbols), CI chondrites (red triangles) and Halley dust (blue squares). The abundances are given relative to iron (Fe) and the figure is adapted from Fig. 2 from (Roberge et al. 2006). The OI detection by Brandeker et al. 2016 who used the Herschel telescope, represents a range of possible values which depend on the spatial distribution of the O gas in the CS disk. The OI column density estimate by Roberge et al. 2006 (represented by the black circle) could represent a lower column density limit due to challenges associated with measuring optically thick OI lines (see Brandeker 2011 and Fig. S1 in Roberge et al. 2006). The CI chondrites consistently show low abundances for the volatile elements H, C, N, O which is expected as they were in a gaseous state when the meteorite formed and did thus not condense or accrete.

values are likely caused by uncertainties in the wavelength solution.

To estimate the total column density of circumstellar NI gas we add the two circumstellar components together:

$$\log(N_{\mathrm{NI}}/1\,\mathrm{cm}^2)_{\mathrm{CS}} = \log\left(10^{\mathrm{NI}_{\mathrm{CS}_0}/1\,\mathrm{cm}^2} + 10^{\mathrm{NI}_{\mathrm{CS}_X}/1\,\mathrm{cm}^2}\right) = 14.9 \pm 0.7 \tag{3}$$

We compare the ratio of the N/Fe column density (normalised to Si) with solar abundances, CI chondrites and Halley dust in Fig. 2. It shows that the NI abundance is consistent with solar and Halley dust abundances, yet is inconsistent with CI chondrites.

4.2. An indirect estimate of the H column density of the ISM in the direction of β Pic

Using the *HST* and the Goddard High Resolution Spectrograph (GHRS), Meyer et al. (1997) conducted observations of the interstellar NI and found a value for the mean interstellar gas-phase N/H abundance at $(7.5 \pm 0.4) \times 10^{-5}$. Furthermore, they reported no statistically significant variations in the measured N abundances from sight line to sight line and no evidence of density-dependent nitrogen depletion from the gas phase. We estimate the total hydrogen column density in the ISM given the value for the NI ISM column density calculated in this paper and assuming N(NI)≈N(N_{total}). From the NI ISM column density we calculate that the HI ISM value in the direction of β Pic is $\log(N_{\mathrm{HI}}/1\,\mathrm{cm}^2)_{\mathrm{ISM}} = 17.9^{+0.2}_{-0.3}$. This is consistent with Wilson et al. (2017) where this value was found to be 18.2 ± 0.1.

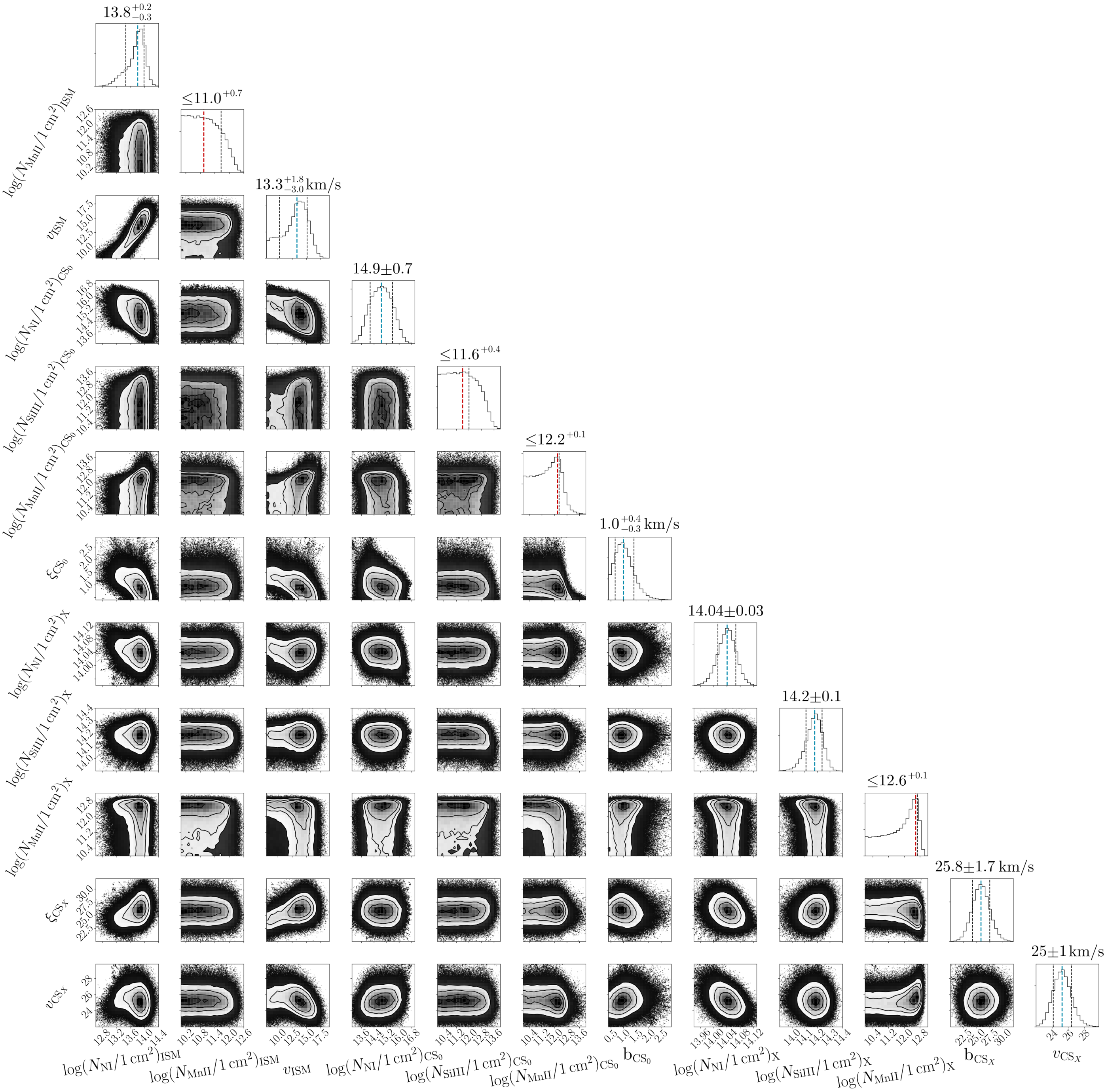

Fig. 3. A corner plot showing the one and two dimensional projections of the posterior probability distributions for the free parameters. The blue dashed lines indicate the mean of the distribution. The black dashed lines in each of the 1D histograms represent the $1\,\sigma$ deviations (68 % of the mass) with the central dashed line indicating the median value. The solid black lines in each of the 2D histograms represent the 1, 2 and $3\,\sigma$ levels respectively (with $1\,\sigma$ = 39.3 % of the volume). The red dashed lines indicate the mode of the distribution. For the parameters which only have an upper uncertainty, the uncertainty was calculated using assuming a truncated Gaussian distribution.

4.3. Column density estimates for MnII and SiII**

We are able to place robust upper limits on the column density estimates for MnII and SiII**. The lower limit is generally unobtainable as the absorption signature is so small that it becomes indistinguishable from the noise. The MnII posterior distributions are not flat topped, however, which one would expect when the absorbing component becomes indistinguishable from the noise. As there seems to be a preferred column density value, we estimate the MnII column density by calculating the mode of the MnII column density distributions and find them to be $12.2^{+0.1}$ and $12.6^{+0.1}$ for the CS$_0$ and CS$_{\rm X}$ components respectively. Added together we get a value of $\log(N_{\rm MnII}/1\,{\rm cm}^2)_{\rm CS} = 12.7 \pm 0.1$ or $(5.0 \pm 1.2) \times 10^{12}$ atoms cm^{-2}. This value is consistent with the value of $3.8{\times}10^{12}$ atoms cm^{-2} reported by Lagrange et al. (1998).

The total SiII** CS column density is dominated by the CS$_{\rm X}$ component which is $\log(N_{\rm SiII^{**}}/1\,{\rm cm}^2)_{{\rm CS}_X} = 14.2 \pm 0.2$ or $(1.6 \pm 0.7) \times 10^{14}$ atoms cm^{-2}. Lagrange et al. (1998) measure a value of 1.1×10^{14} atoms cm^{-2} which is also consistent with our measurement.

5. Discussion

5.1. Implications of a solar NI abundance

The column density of NI relative to iron is shown in Fig. 2. The NI column density is consistent with solar abundances, unlike C and O, which are overabundant.

The *preferential depletion* scenario presented in Xie et al. (2013) suggest the overabundance of C and O is due to their accumulation in the disk. As the radiation from β Pic depletes the metallic elements (susceptible to radiation pressure), such as Na, Mg, Ca and Fe, the radiation resilient species remain in the gas disk resulting in an C and O overabundance. Under such a scenario one would expect N to also be overabundant, as N has a low sensitivity to radiation pressure, like C and O. This can be demonstrated by evaluating the ratio of the radiation pressure to stellar gravity, which is expressed as β:

$$\beta = \frac{d^2}{GmM_\star}\frac{1}{4\pi\epsilon_0}\frac{\pi e^2}{m_e c^2} f\phi_\nu \tag{4}$$

where d is the distance to the star, G is the gravitational constant, m is the mass of the ion under consideration, $M_\star$ is the stellar mass, ϵ_0 the permittivity of free space, e the elementary charge, m_e the mass of the electron, c the speed of light, f the oscillator strength of the transition and ϕ_ν the stellar flux at the considered wavelength (per unit frequency). We calculate this quantity using the following values: $f = 0.130$ (for the strongest line), $m = 14\,\mathrm{u}$, $\lambda = 1199.55$ Å, stellar flux = 1.0×10^{-14} erg/s/cm^2/Å, $d = 19.3$ pc, and $M_\star = 1.75 M_\odot$. This returns $\beta \simeq 3.6 \times 10^{-4}$. While determining the exact influence of radiation pressure on nitrogen atoms would require a dynamical model, such a low value for β indicates that it should have a negligible effect. Despite these minimal effects from radiation pressure, we do not find an overabundance of nitrogen in the β Pictoris disk. Other papers have also shown no clear deficiency in radiation sensitive species such as Na and Ca (Lagrange et al. 1998), which also seems to disfavour the preferential depletion scenario.

The *preferential production* scenario, also proposed by Xie et al. (2013), suggests that the overabundance is the result of gas being produced from materials rich in C and O. This includes photodesorption from C and O-rich icy grains (Grigorieva et al. 2007) and collisional vaporisation of the dust in the disk (Czechowski & Mann 2007). Unlike preferential depletion, this scenario does not infer high N abundances and is thus more compatible with the near-solar NI abundance measured here.

5.2. The origin and dynamics of the NI gas

The absorption components which we use to model the shape of the NI absorption lines may provide us with hints at both the origin and dynamics of the NI gas. The two absorbing circumstellar components, CS$_0$ and CS$_X$, were not constrained to particular radial velocity values, yet provided the best fit when their radial velocities matched that of the star. This indicates an absence of detectable amounts of NI falling in towards the star. The clearly asymmetric HI Ly-α line presented in Wilson et al. (2017) on the other hand, indicates that HI gas is falling in towards the star. The HI gas is thought to be originating from the dissociation of water molecules from evaporating exocomets. The fact that we do not see similar asymmetric line profiles in NI is perhaps not surprising. In Solar System comets, nitrogen-bearing molecules are only minor constituents (Eberhardt et al. 1987), so if β Pic comets are similar, we would not expect the NI lines to be asymmetric. This does, however, not exclude the possibility that NI might originate from exocomets, as we argue in §5.3.

5.3. The role of exocomets

The NI column density measurements are dominated by the narrow absorption feature, CS$_0$, which has a line width of $b_{\mathrm{CS}_0} \sim 1$ km/s. With a similar line width observed in FeI (Vidal-Madjar et al. 2017), this absorption feature likely traces a stable band of circumstellar material orbiting β Pic. The origin of the broad absorption feature, CS$_X$, with $b_{\mathrm{CS}_X} \sim 26$ km/s which absorbs 7× less but clearly governs much of the absorption line shape is less clear. It may be the case that the feature consists of a number of individual absorption components which are outside the resolving powers of the COS instrument.

The broad component could be related to NI absorption lines in the stellar atmosphere of β Pic. This would certainly explain the bulk velocity matching that of the star. However, we would then expect the lines to be much broader and shallower due to the rapid rotation of β Pic at ~ 130 km/s (Royer et al. 2007). In any case, a slight contamination of the line by absorption in the stellar atmosphere would not alter significantly the final NI column density and the subsequent conclusion.

Another possibility is that the component is caused by gas which originated from exocomets and which has accumulated over time. Although exocomets are unlikely to be rich in nitrogen, there may have been a build up of NI from successive cometary visits over time. The NI which does originate from comets is not going to be very sensitive to radiation pressure, and thus may linger for longer in the system. This could explain the stability of the feature and the width of the line resulting from the velocity distribution of the evaporating comets which over time deposit the NI.

The exocomets in the β Pic disk can be categorised into two separate populations with different dynamical properties (Kiefer et al. 2014). The first population (population S) consists of exocomets that produce shallow absorption lines at high radial velocities (~ 40 km/s and above), which are attributed to exhausted exocomets trapped in a mean motion resonance with β Pic b. The second population consists of exocomets producing deep absorption lines at low radial velocities, which could be related to the recent fragmentation of one or a few parent bodies. The comets which may contribute to the wide absorption feature seen here would originate from this latter population (population D). The velocity distribution of these comets has a FWHM of 15 ± 6 km/s. This line width is similar to that of the broad absorption feature, suggesting that the build-up of gas in cometary debris streams from this population may explain the line's large width. Interestingly, if the exocomets fragment, the rates at which NI is produced could be higher.

6. Conclusions

We measure the column density of neutral nitrogen in the β Pictoris circumstellar disk for the first time, and find it to be $\log(N_{\mathrm{NI}}/1\,\mathrm{cm}^2) = 14.9 \pm 0.7$. Comparing the abundance ratio of NI relative to Fe in the β Pic disk we obtain a result consistent with both solar and Halley dust abundance ratios. In addition, we measure an upper limit for the MnII column density in the disk to be $\log(N_{\mathrm{MnII}}/1\,\mathrm{cm}^2)_{\mathrm{CS}} = 12.7^{+0.1}$ and measure SIII** to be $\log(N_{\mathrm{SIII}^{**}}/1\,\mathrm{cm}^2)_{\mathrm{CS}} = 14.2 \pm 0.1$, which agrees well with previous estimates.

The near-solar abundance ratio of NI to Fe favours the preferential production scenario which suggests the gas surrounding β Pic is naturally rich in C and O. We detect two distinct absorption components; a high column density and narrow component which we attribute to a stable band of circumstellar material orbiting *β Pic* and a broader, lower column density component which we suggest could be due to the successive build up of NI which originates from exocomets.

Acknowledgements. P.A.W, A.L.E and A.V-M all acknowledge the support of the French Agence Nationale de la Recherche (ANR), under program ANR-12-BS05-0012 "Exo-Atmos". P.A.W. and I.S. acknowledge support from the European Research Council under the European Unions Horizon 2020 research and innovation programme under grant agreement No. 694513. This project has been carried out in part in the frame of the National Centre for Competence in Research PlanetS supported by the Swiss National Science Foundation (SNSF), and has received funding from the European Research Council (ERC) under the European Union's Horizon 2020 research and innovation programme (project Four Aces; grant agreement No 724427). F.K. is funded by a CNES fellowship. A.L.E, A.V-M and F.K thank the CNES for financial support P.A.W would like to thank Luca Matrà and Grant Kennedy for fruitful and inspiring discussions.

References

Akaike, H. 1974, IEEE transactions on automatic control, 19, 716
Bertin, P., Vidal-Madjar, A., Lallement, R., Ferlet, R., & Lemoine, M. 1995, A&A, 302, 889
Beust, H., Vidal-Madjar, A., Ferlet, R., & Lagrange-Henri, A. M. 1990, A&A, 236, 202
Bourrier, V., Ehrenreich, D., Lecavelier des Etangs, A., et al. 2018, A&A, 615, A117
Brandeker, A. 2011, ApJ, 729, 122
Brandeker, A., Cataldi, G., Olofsson, G., et al. 2016, A&A, 591, A27
Brandeker, A., Liseau, R., Olofsson, G., & Fridlund, M. 2004, A&A, 413, 681
Czechowski, A. & Mann, I. 2007, ApJ, 660, 1541
Dent, W. R. F., Wyatt, M. C., Roberge, A., et al. 2014, Science, 343, 1490
Eberhardt, P., Krankowsky, D., Schulte, W., et al. 1987, A&A, 187, 481
Ferlet, R., Vidal-Madjar, A., & Hobbs, L. M. 1987, A&A, 185, 267
Fernández, R., Brandeker, A., & Wu, Y. 2006, ApJ, 643, 509
Foreman-Mackey, D. 2016, The Journal of Open Source Software, 24
Foreman-Mackey, D., Hogg, D. W., Lang, D., & Goodman, J. 2013, PASP, 125, 306
Fox et al. 2015, COS Data Handbook, Version 3.0 (Baltimore: STScI)
Gontcharov, G. A. 2006, Astronomical and Astrophysical Transactions, 25, 145
Grigorieva, A., Thébault, P., Artymowicz, P., & Brandeker, A. 2007, A&A, 475, 755
Hobbs, L. M., Vidal-Madjar, A., Ferlet, R., Albert, C. E., & Gry, C. 1985, ApJ, 293, L29
Jones, E., Oliphant, T., Peterson, P., et al. 2001–, SciPy: Open source scientific tools for Python, [Online; accessed 13. Sept. 2018]
Kral, Q., Matrà, L., Wyatt, M. C., & Kennedy, G. M. 2017, MNRAS, 469, 521
Kral, Q., Wyatt, M., Carswell, R. F., et al. 2016, MNRAS, 461, 845
Krankowsky, D., Lämmerzahl, P., Herrwerth, I., et al. 1986, Nature, 321, 326
Lagrange, A. M., Beust, H., Mouillet, D., et al. 1998, A&A, 330, 1091
Lallement, R., Ferlet, R., Lagrange, A. M., Lemoine, M., & Vidal-Madjar, A. 1995, A&A, 304, 461
Lecavelier Des Etangs, A., Vidal-Madjar, A., & Ferlet, R. 1996, A&A, 307, 542
Mamajek, E. E. & Bell, C. P. M. 2014, MNRAS, 445, 2169
Matrà, L., Dent, W. R. F., Wyatt, M. C., et al. 2017, MNRAS, 464, 1415
Meyer, D. M., Cardelli, J. A., & Sofia, U. J. 1997, ApJ, 490, L103
Roberge, A., Feldman, P. D., Lecavelier des Etangs, A., et al. 2002, ApJ, 568, 343
Roberge, A., Feldman, P. D., Weinberger, A. J., Deleuil, M., & Bouret, J.-C. 2006, Nature, 441, 724
Roberge, A., Welsh, B. Y., Kamp, I., Weinberger, A. J., & Grady, C. A. 2014, ApJ, 796, L11
Royer, F., Zorec, J., & Gómez, A. E. 2007, A&A, 463, 671
Schwarz, G. et al. 1978, The annals of statistics, 6, 461
Vidal-Madjar, A., Kiefer, F., Lecavelier des Etangs, A., et al. 2017, A&A, 607, A25
Vidal-Madjar, A., Lagrange-Henri, A.-M., Feldman, P. D., et al. 1994, A&A, 290, 245
Visser, R., van Dishoeck, E. F., & Black, J. H. 2009, A&A, 503, 323
Wilson, P. A., Lecavelier des Etangs, A., Vidal-Madjar, A., et al. 2017, A&A, 599, A75
Wyckoff, S., Tegler, S. C., & Engel, L. 1991, ApJ, 367, 641
Xie, J.-W., Brandeker, A., & Wu, Y. 2013, ApJ, 762, 114
Zuckerman, B. & Song, I. 2012, ApJ, 758, 77

Appendix A: Airglow Subtraction

Appendix A.1: Creation of an airglow-free template

Before subtracting the airglow, we created a reference spectrum of airglow-free data to determine the amount of airglow that had to be subtracted for each observation. The amount of airglow contamination varies as a function of HST orbital position and not all of the spectra are noticeably affected by airglow. The airglow contamination is mostly dependent on the Sun-Earth-target angle followed by the amount of terrestrial atmosphere which HST observes through (which depends on the angle between the centre of the Earth and the target). Some of the observations show relatively minor contamination by airglow, and we use them to create this reference spectrum.

We use the airglow-dominated Ly-α emission feature to identify the observations with minimal airglow (Bourrier et al. 2018), and classify observations with a peak Ly-α flux of less than $1 \times 10^{-12}\mathrm{ergs}^{-1}\mathrm{cm}^{-2}\mathrm{Å}^{-1}$ as containing negligible airglow effects in the nitrogen triplet. A weighted average of spectra with negligible airglow contamination was then computed. The average of these spectra was treated as an *airglow-free* template, which we use as a reference to check the that the airglow contamination was correctly subtracted from the remaining airglow-contaminated data. The airglow-free template was smoothed by applying a linear convolution filter with a smoothing scale of 12 pix (0.02 Å 4.3 km/s), somewhat larger than the line spread function (LSF) of the instrument, which has a FWHM of roughly 7 pix. The smoothed airglow-free template thus avoids the introduction of localised noise variations which occur on smaller pixel length scales.

Appendix A.2: Calculating the scaling factor, C

Once the airglow-free spectrum was generated, it was aligned to the airglow-contaminated data, as was the airglow template. Since the airglow and airglow-free spectra have different sets of visible spectral features, they had to be aligned to each airglow-contaminated spectrum using different sets of lines. The airglow template, F_{AG}, could not be directly aligned to the airglow around the NI triplet, as the airglow emission was much weaker than the much deeper NI absorption components. Using instead the airglow-dominated Lyman α (Ly-α) line (16 Å away) proved to be a much more reliable alignment reference, reliably aligning the NI airglow emission excess. A second-order polynomial was fit to the top part of the Ly-α emission line (±120 km/s), which was present in all spectra. The wavelength position of the peak of the polynomial used to quantify the line position.

With the airglow template aligned to the airglow-contaminated data, the airglow-free template could be included. The cross correlation method presented in Section 3.1 of Wilson et al. (2017) was applied in the vicinity of the NI lines (1199.4-1201.0 Å) to align the airglow-free template, the airglow-contaminated spectra and airglow spectrum for each of the airglow-contaminated observation sets. The result was that after this alignment, the airglow template was aligned to the airglow in the contaminated spectrum, and the emission lines in the contaminated spectrum were aligned to the airglow-free template's emission lines. This alignment was successful for all but one, especially noisy, spectrum from the April 22, 2017 observation, which was left out of this analysis.

With both templates properly aligned to the data, we finally apply Equation 1. For each airglow-contaminated observation, C was calculated by minimising the residuals between the two sides of Equation 1 around the NI triplet, using the averaged airglow-free model as F. Once C was determined, F was recomputed using Equation 1, finally resulting in airglow-subtracted observations, which are used in the subsequent analysis.

Appendix A.3: Airglow subtraction verification

We aligned the spectra taken at different epochs using the cross correlation method mentioned in Section 3.1 (Wilson et al. 2017). We initially chose the region of 1249 to 1255 Å, which is centred on a pair of SII lines, due to its favourable signal-to-noise ratio and the lack of transient exocometary sulphur features (e.g. Roberge et al. 2002, 2014). However, upon close inspection, it was found that slight radial velocity deviations existed between different lines of the same species at the same epoch (e.g. SiII, C I). We therefore conclude that wavelength solution errors exist, and that it is consequently best to align to features as close to the desired region as possible. Since the NI lines themselves (1199.4-1201.0,Å) showed minimal evidence of red or blue-shifted cometary absorption features, we decided to align to them directly, thereby avoiding any wavelength solution problems.

All spectra were aligned and normalized to the first spectrum taken on 24 February 2014. The normalisation was done by comparing the median flux value for all of the spectra across a wavelength range redward of the NI triplet (1210.0 to 1214.0 Å), known to be void of airglow and strong spectral lines. No misalignment was evident upon visual analysis, so we concluded that the alignment was successful and combined all airglow-subtracted spectra through a weighted average. This combined spectrum did not show a different shape or width compared to those of the individual observations, further verifying the quality of the alignment. This produced the final spectrum that we analyse in this paper.